Journal of Alloys and Compounds 805 (2019) 909–914

Contents lists available at ScienceDirect

Journal of Alloys and Compounds

journal homepage: http://www.elsevier.com/locate/jalcom

Tuning the magnetic and structural properties of a three-metal boride alloy: $Mn_{0.95-\delta}Fe_{1.05+\delta-x}Co_xB$

Mykola Abramchuk, Thomas Mier, Fazel Tafti*

Department of Physics, Boston College, Chestnut Hill, MA, 02467, USA

ARTICLE INFO

Article history:
Received 3 April 2019
Received in revised form
26 June 2019
Accepted 11 July 2019
Available online 13 July 2019

Keywords:
boride
Alloys
Crystallography
Magnetism
Magnetocaloric

ABSTRACT

We present a comprehensive study of the three-metal boride alloys $Mn_{0.95-\delta}Fe_{1.05+\delta-x}Co_xB$ ($\delta = 0 - 0.15$ and $x = 0 - 1.05$) synthesized via arc melting and annealing. The alloys crystallize in a body-centered tetragonal unit cell in the same space group ($I4/mcm$) as the parent compound Mn_2B. A small amount of MB (M = Mn, Fe, Co) impurity forms in the as-cast samples which is removed by acid treatment. Rietveld refinement on the powder X-ray data reveals an anisotropic variation of lattice parameters in the series. The *c*-axis increases with increasing Co content but the *a*-axis decreases. Magnetic measurements show a non-monotonic variation of both T_c and the saturated magnetization M_s as a function of *x*. These findings highlight the tunable nature of $Mn_{0.95-\delta}Fe_{1.05+\delta-x}Co_xB$ and motivate further studies of metal-rich boride alloys.

1. Introduction

Boron is the only non-metal element in group 13 of the periodic table. It shows more similarities to its right neighbor, carbon, with the important difference that boron has one less valence electron than the number of valence orbitals. This electron deficiency, together with boron's electronegativity and small size, lead to a combination of boron-boron and boron-metal bonds that are responsible for the remarkable structural diversity of transition metal borides (TMBs) [1]. Binary TMBs can range from M_4B to MB_{50} stoichiometry, from tetrahedral to icosahedral coordination polyhedra, and from isolated boron atoms in a metallic framework to isolated metal atoms in a boron framework [2,3]. Despite a large body of research on the structural properties of borides, their applications have hitherto been quite limited. Recent efforts have been undertaken to unveil the applicable physical properties of borides. Two discernible examples are the observation of a sizable magnetocaloric effect in $AlFe_2B_2$ [4,5] and the advent of super-hard or ultra-incompressible alloys [6,7]. In this work, we present another applicable aspect of borides, namely the tunable nature of magnetism in three-metal TMB alloys.

One of the best studied families of TMBs are M_2B systems (M can be Mn, Fe, Co, or Ni). The present work was motivated by the structural similarity between Mn_2B, Fe_2B, and Co_2B that crystallize in the Al_2Cu structure-type with a tetragonal unit cell in the space group $I4/mcm$ [8–10]. Fig. 1 shows two different views of the M_2B structure. In Fig. 1a, transition metals form a distorted tunnel structure and boron atoms form 1D chains. In Fig. 1b, one transition metal and four borons form capped pyramids with alternating directions along the *c*-axis due to the *c*-glide planes. Prior attempts to tune the properties of M_2B family have been limited to two-metal alloys such as $(Co_{1-x}Mn_x)_2B$, $(Fe_{1-x}Mn_x)_2B$, and $(Fe_{1-x}Co_x)_2B$ [11–13]. Similarly, two-metal alloys have been explored in the MB family, such as $Mn_{1-x}Co_xB$ and $Mn_{1-x}Fe_xB$ [14,15]. Our objective was to go beyond the simple two-metal alloys and synthesize a series of three-metal alloys in the M_2B structural family, to achieve a higher level of structural complexity. As a result, a solid solution of $Mn_{0.95-\delta}Fe_{1.05+\delta-x}Co_xB$ was synthesized with $\delta = 0 - 0.15$ and $x = 0 - 1.05$. We found that both transition temperature (T_c) and the saturated magnetization (M_s) were tuned in parallel as a function of *x*.

2. Experimental methods

2.1. Material synthesis

The samples of $Mn_{0.95-\delta}Fe_{1.05+\delta-x}Co_xB$ ($\delta = 0 - 0.15$ and $x = 0 - 1.05$) were synthesized by arc melting method using powders of manganese (Aldrich, 99.99%), cobalt (Alfa Aesar, 99.5%), crystalline

* Corresponding author.
E-mail address: fazel.tafti@bc.edu (F. Tafti).

https://doi.org/10.1016/j.jallcom.2019.07.119
0925-8388/

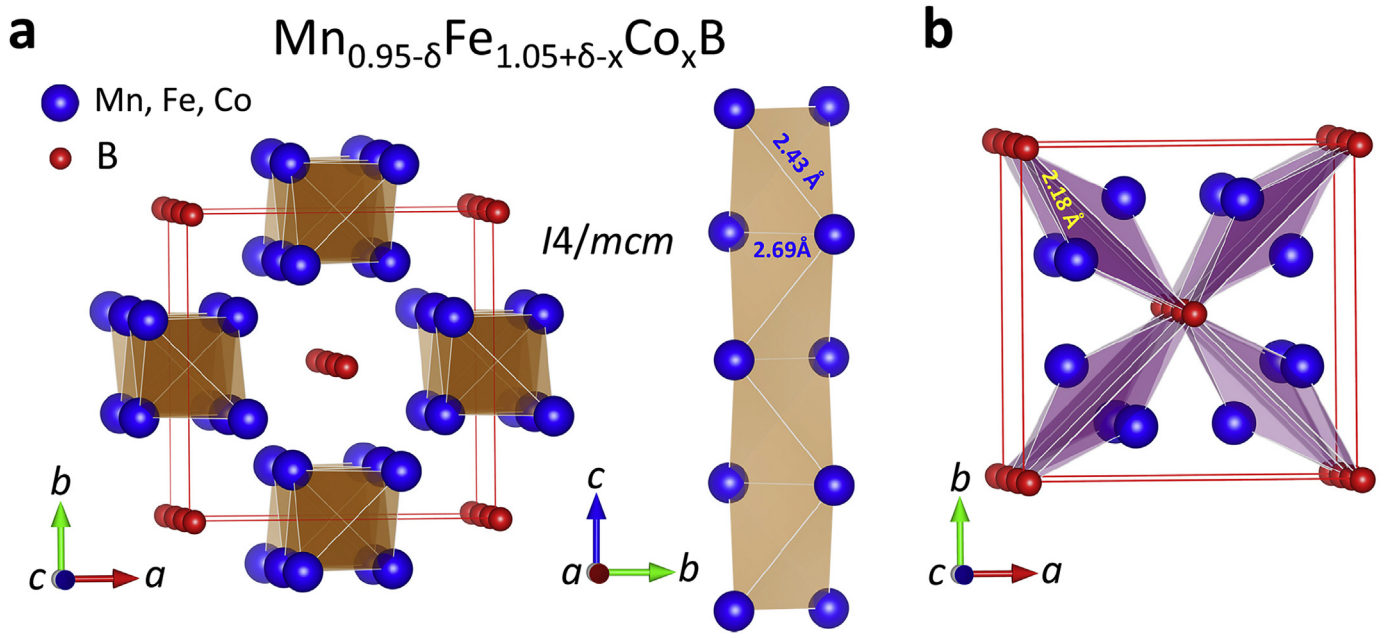

Fig. 1. (a) The crystal structure of M_2B can be viewed as a body-centered tetragonal unit cell with 1D chains of boron atoms stacked along the edges and center of the unit cell. The transition metals form a tunnel structure of tetrahedral units along the edge centers. (b) A different view of the M_2B structure showing the shortest bond distance between the transition metal and boron atoms (2.18 Å). Each M-atom is bonded to four B-atom in a non-coplanar square geometry. The reported bondlengths on this figure belong to $Mn_{0.91}Fe_{0.55}Co_{0.54}B$.

boron (Alfa Aesar, 98%), and iron (Alfa Aesar 99.9%). To eliminate oxide impurities, metal powders were first annealed under the flow of a reducing gas mixture (5% H_2/Ar) at 500 °C for 5 h. The stoichiometric mixtures of starting components with total mass of 350 mg were pressed into 6 mm diameter pellets and arc-melted under inert argon atmosphere. A 6.5% excess of boron was added to compensate for losses of boron at the arc melting stage and to avoid formation of metal-rich impurity phases. Each ingot was turned over and re-melted 3 times to obtain a homogeneous specimen. The ingots were subsequently annealed at 1000 °C for 5 days while being wrapped in molybdenum foil (Alfa Aesar, 99.95%, 0.025 mm thickness) inside evacuated quartz tubes. Finally, samples were ground into fine powders and washed in diluted hydrochloric acid (1:1 v/v) for 200 min to remove a byproduct of MB phase. The preparation of the initial mixtures and pellets was performed in an argon glovebox with O_2 and H_2O content <0.1 ppm. The final samples were found to be robust in air with no changes of physical appearance or X-ray pattern after several weeks at ambient conditions.

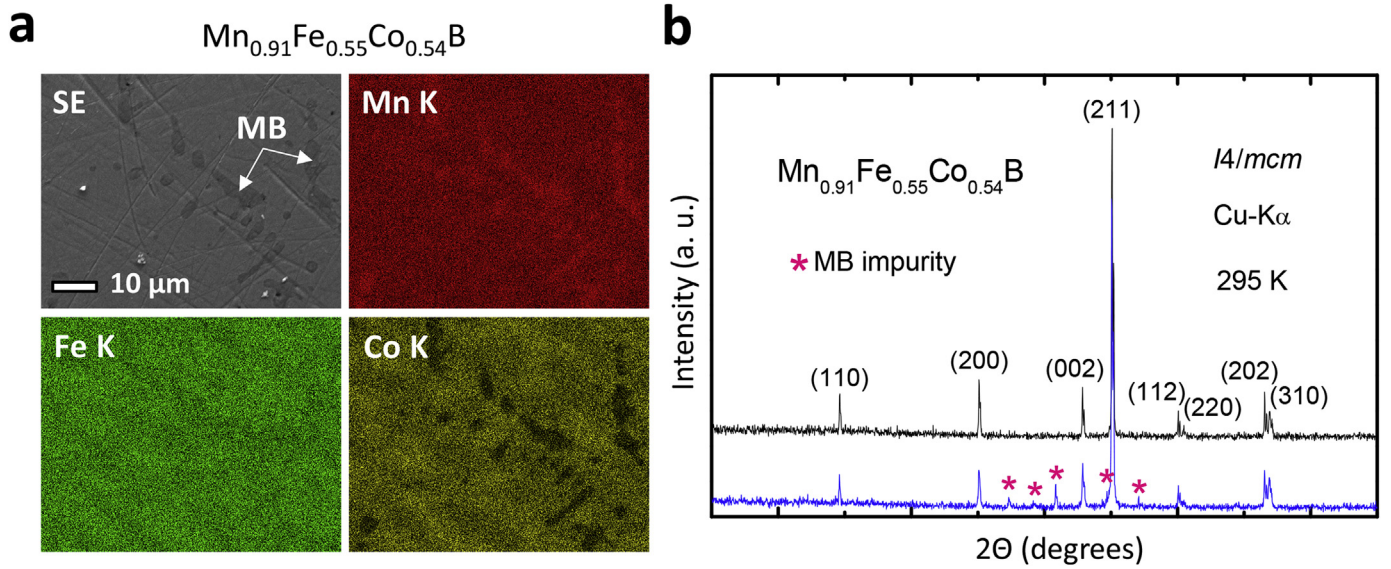

Fig. 2. (a) SEM image from a representative sample with the composition $Mn_{0.91}Fe_{0.55}Co_{0.54}B$. Color maps show the distribution of Mn, Fe, and Co across the field of view. The MB impurity phase (M = Mn, Fe, Co) is characterized by a different contrast in both the secondary electron (SE) image and the color maps. (b) PXRD patterns from the representative sample, before (blue) and after (black) acid treatment with dilute HCl (1:1 v/v, 200 min) The MB impurity peaks are completely vanished after acid treatment in Co-rich samples. However, the MB impurity is slightly more resilient in Fe-rich samples (Supplemental Fig. S1). (Colors appear in the Web version.)

2.2. Electron microscopy

Scanning electron microscopy (SEM) and energy-dispersive X-ray spectroscopy (EDX) were performed using a Zeiss Ultra-55 field emission electron microscope (FESEM), operating at 20 kV and equipped with an EDAX detector. Prior to the SEM investigations, all as-cast specimens were polished to achieve a flat sample surface suitable for EDX analysis.

2.3. X-ray diffraction

Room temperature powder X-ray diffraction (PXRD) was performed in reflection (Bragg-Brentano) geometry using a Bruker D8 ECO diffractometer equipped with a copper K_α source, a nickel filter to absorb K_β radiation, and 2.5° Soller slits after the source and before the LYNXEYE XE 1D energy-dispersive detector. The WinCSD software was used for the Rietveld refinement [16].

Table 1
EDX results tabulated for 10 compositions of $Mn_{0.95-\delta}Fe_{1.05+\delta-x}Co_xB$ in this study. Acid treatment was used to eliminate the MB impurity phase (see the results below).

Nominal composition	EDX result	Result of HCl treatment
MnFeB	$Mn_{0.94(1)}Fe_{1.06(1)}B$	trace of MB
$MnFe_{0.9}Co_{0.1}B$	$Mn_{0.92(1)}Fe_{0.99(1)}Co_{0.08(1)}B$	6.13% of MB
$MnFe_{0.8}Co_{0.2}B$	$Mn_{0.95(1)}Fe_{0.86(1)}Co_{0.19(1)}B$	pure sample
$MnFe_{0.7}Co_{0.3}B$	$Mn_{0.95(1)}Fe_{0.76(1)}Co_{0.29(1)}B$	pure sample
$MnFe_{0.6}Co_{0.4}B$	$Mn_{0.96(2)}Fe_{0.64(1)}Co_{0.39(1)}B$	pure sample
$MnFe_{0.5}Co0.5B$	$Mn_{0.91(1)}Fe_{0.55(1)}Co_{0.54(1)}B$	pure sample
$MnFe_{0.4}Co_{0.6}B$	$Mn_{0.93(4)}Fe_{0.45(1)}Co_{0.63(3)}B$	trace of MB
$MnFe_{0.3}Co_{0.7}B$	$Mn_{0.80(3)}Fe_{0.36(1)}Co_{0.84(2)}B$	pure sample
$MnFe_{0.2}Co_{0.8}B$	$Mn_{0.91(2)}Fe_{0.21(1)}Co_{0.89(2)}B$	pure sample
MnCoB	$Mn_{0.95(2)}Co_{1.05(2)}B$	pure sample

2.4. Magnetic measurements

DC magnetization measurements were performed using a 7 T Quantum Design MPMS3 between 1.8 and 400 K on polycrystalline samples in the low-background brass holders. To evaluate the magnetocaloric effect (MCE), magnetization isotherms where collected in the temperature range T_c±50 K with 2 K steps and the magnetic entropy change (ΔS_M) was calculated using the Maxwell equation [17].

$$\Delta S_M(T, \Delta H) = \int_0^{H_{max}} \left(\frac{\partial M}{\partial T}\right)_H dH \quad (1)$$

which was approximated with the following expression for discrete isotherms:

$$\Delta S_M\left(T = \frac{T_1 + T_2}{2}\right) = \left(\frac{1}{T_2 - T_1}\right) \times \left[\int_0^{H_{max}} M(T_2, H)dH - \int_0^{H_{max}} M(T_1, H)dH\right] \quad (2)$$

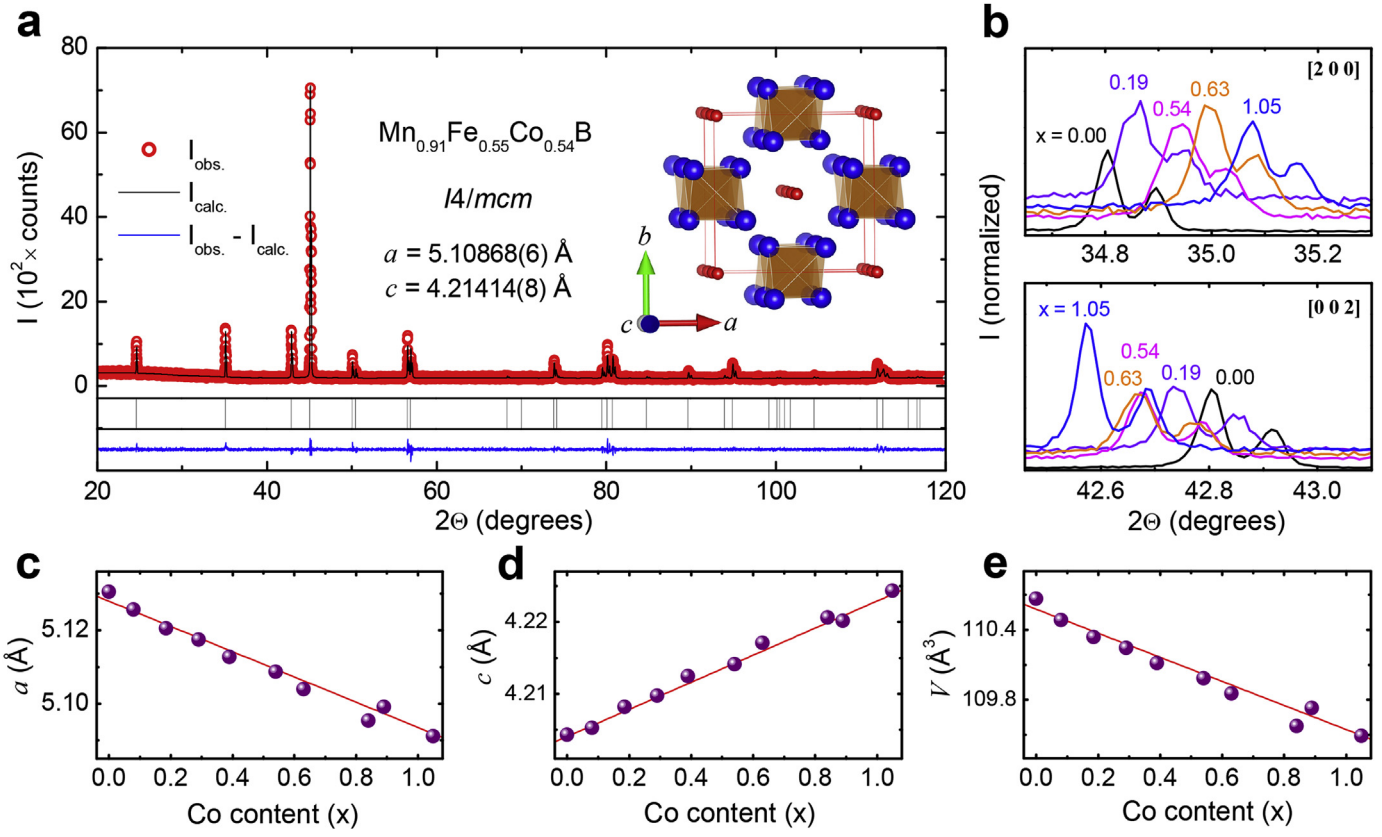

Fig. 3. (a) Representative Rietveld refinement of a $Mn_{0.95-\delta}Fe_{1.05+\delta-x}Co_xB$ sample with $x = 0.54$. In this refinement, $R_I = 0.0466$, $R_{wp} = 0.0764$, and $\chi^2 = 1.377$ (see Supplemental information for the refinement parameters of all samples). (b) Systematic disposition of [200] peaks toward higher angles and [002] peaks toward lower angles. (c,d,e) Lattice parameters a and c, and unit cell volume $V = a^2c$ plotted as a function of x in $Mn_{0.95-\delta}Fe_{1.05+\delta-x}Co_xB$.

2.5. Electronic structure calculations

Calculations of non-polarized electronic density of states (DOS) for Mn_2B, Fe_2B, MnFeB and MnCoB were performed using the tight-binding linear muffin-tin orbitals atomic sphere approximation (TB-LMTO-ASA) software [18]. The available room-temperature crystallographic data [8,11,19,20] were used as the starting input information. The integration was performed using a 16 ×16× 16 *k*-mesh.

3. Results and discussion

3.1. Compositional analysis

Since this is the first presentation of a three-metal M_2B alloy, we thoroughly analyzed both the composition and structure of the samples. Table 1 summarizes the results of our EDX measurements on 10 samples, reporting both their nominal (synthetic target) and actual (evaluated by EDX) compositions. Notice that all samples have a slight Mn-deficiency and Fe-excess compared to their nominal compositions, hence the chemical formula $Mn_{0.95-\delta}Fe_{1.05\ +\ \delta-x}Co_xB$. This off-stoichiometry results from the formation of an MB impurity phase where M is predominantly Mn (mixed with Co and Fe). For example, Fig. 2a reveals the MB impurity in EDX color maps from an as-cast sample of $Mn_{0.91}Fe_{0.55}Co_{0.54}B$. PXRD pattern from the same sample (blue data in Fig. 2b) also confirms this impurity. We succeeded to remove the MB impurity by grinding the samples and immersing them in dilute hydrochloric acid (1:1 v/v) for 200 min. This suggests that the target phase M_2B reacts with HCl at a slower rate compared to the impurity phase MB. Recent work [4] has demonstrated that it is not possible to remove iron monoboride impurity (FeB) from the metal-rich boride $AlFe_2B_2$ by acid treatment, because single-metal monoborides MB are typically robust against HCl. Thus, our results indicate that the chemical stability of M_2B and MB phases is sensitive to the ratio of metals mixed in the structure – an interesting subject for further chemical investigations.

3.2. Crystal structure

PXRD patterns from all samples were perfectly indexed in the tetragonal unit cell *I*4 /*mcm*, except for trace amounts of MB impurity (Table 1). Fig. 3a shows the PXRD pattern and the Rietveld refinement on a representative sample $Mn_{0.91}Fe_{0.55}Co_{0.54}B$ – a composition in the middle of the $Mn_{0.95-\delta}Fe_{1.05\ +\ \delta-x}Co_xB$ series. The absence of superstructure peaks confirms a homogeneous mixture of Mn, Fe, and Co in the Wyckoff site 8*h*. Note that it is not possible to reliably determine the Mn, Fe, and Co contents from X-ray data due to their close atomic form factors. One approach to rectify this problem is to use Neutron scattering and take advantage of the different scattering length of Mn, Fe, and Co. However, neutron experiments require a large amount of material which is difficult to prepare using a laboratory-scale arc melting furnace. Therefore, we took a different approach and used the compositions obtained by the EDX to fix the occupancy of the site 8*h* in the Rietveld analysis assuming that both metal and boron sites are fully occupied. The complete set of lattice parameters, refinement *R*-factors, atomic positions, and thermal factors for each sample is provided in the Supplemental information (Tables S1–S4). Fig. 3b shows a systematic drift of [*h*00] peaks toward higher angles and [00ℓ] peaks toward lower angles, indicating a decreasing *a*-axis

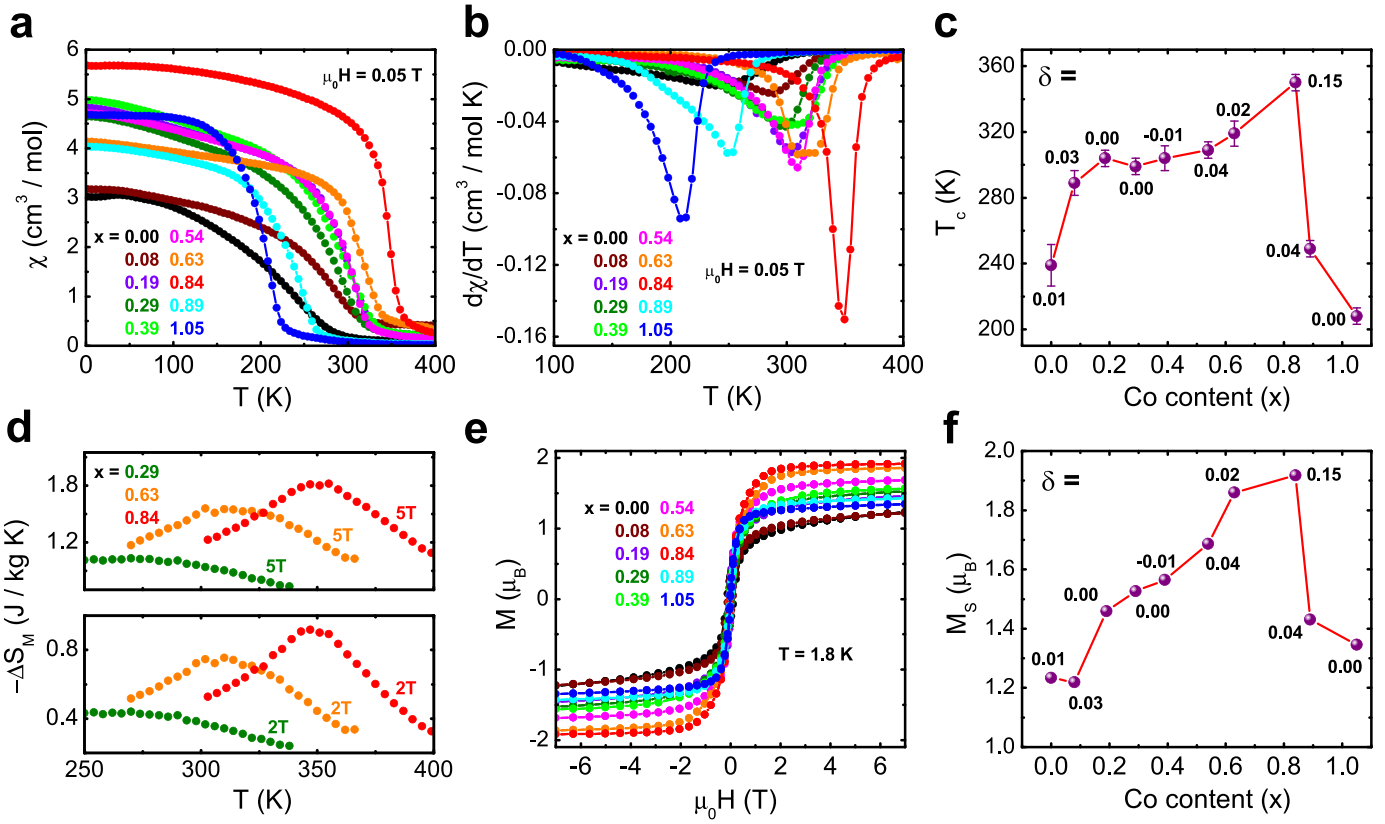

Fig. 4. (a) Magnetic susceptibility (χ) as a function of temperature in ten samples studied here. (b) For each sample, T_c is determined from a peak in $d\chi/dT$. (c) T_c is plotted as a function of Co content (*x*). δ for each $Mn_{0.95-\delta}Fe_{1.05\ +\ \delta-x}Co_xB$ sample is reported on the figure. (d) Change of magnetic entropy ΔS_M as a function of temperature for a field change of 2 and 5 T in three representative samples. (e) Magnetization as a function of field. (f) Saturated magnetization M_s as a function of Co content.

despite an increasing *c*-axis with increasing Co content (x). This anisotropic variation of lattice parameters is highlighted in Fig. 3c and d where the lattice parameters obtained by Rietveld refinements are plotted as a function of Co content. Note that the relative changes of lattice parameters are small and the unit cell volume decreases monotonically with increasing x (Fig. 3e) as expected from the substitution of Fe with Co.

3.3. Magnetic properties

Following the compositional and structural analysis of $Mn_{0.95-\delta}Fe_{1.05+\delta-x}Co_xB$ alloys, we now turn to their magnetic properties. Fig. 4a presents DC magnetic susceptibility as a function of temperature in all samples. The ferromagnetic (FM) transition temperature (T_c) of each sample is determined from a peak in $d\chi/dT$ data (Fig. 4b), and plotted as a function of x in Fig. 4c. We examined the change of magnetic entropy ΔS_M, i.e. the magnetocaloric effect (MCE), in three representative samples with T_c near the room temperature ($x = 0.29$, 0.63, and 0.84). MCE was calculated using Eq. (2) from the $M(H)$ data provided in the Supplemental Fig. S2. Fig. 4d shows a relatively weak MCE in the three samples but the magnitude of ΔS_M increases with increasing T_c. The largest MCE is observed in the sample with $x = 0.84$ and $T_c = 355$ K, where $\Delta S_M = 1.8$ J/kg K for a change in field from 0 to 5 T. This is comparable to the MCE observed in the neodymium-based alloy $Nd(Mn_{1-x}Fe_x)_2Ge_2$ [21]. The effect is clearly visible, although its magnitude is smaller compared to the benchmark materials such as $Gd_5Si_2Ge_2$ and $MnFeP_{0.45}As_{s0.55}$ with $\Delta S_M \approx 18$ J/kg K [22,23]. Fig. 4e presents the magnetization curves (M vs. H), from which, we extract the saturated moment in each sample and plot it as function of x in Fig. 4f. Fig. 4c,f reveal a parallel dome-shape variation of T_c and the saturated moment $\mu = M_s/\mu_B$ as a function of x in $Mn_{0.95-\delta}Fe_{1.05+\delta-x}Co_xB$. The sample with the largest T_c, also has the largest magnetic moment, and the largest magnetocaloric effect. These variations imply a special FM arrangement in the $Mn_{0.95-\delta}Fe_{1.05+\delta-x}Co_xB$ alloys due to a range of magnetic moments from different transition metals on site 8*h*. However, instead of a localized picture, we use an itinerant picture and discuss the variation of both T_c and M_s based on the joint density of states in the next section.

3.4. Electronic structure

The non-monotonic dome-shape dependence of both T_c and M_s on x in Fig. 4c,f can be qualitatively explained from density of states (DOS) calculations in Fig. 5. Because metal-rich borides are itinerant magnets, the density of states at the Fermi level $N(E_F)$ controls the magnetism. For example, Fig. 5a shows that E_F is at a local minimum of DOS in Mn_2B which explains the observed Pauli paramagnetism [12,15]. In contrast, Fig. 5b shows that E_F coincides with a peak (Van Hove singularity) in Fe_2B which explains the ferromagnetic ordering at $T_c = 1010$ K [12,15]. Fig. 5a and b confirm that the gradual increase of $N(E_F)$, due to increasing electron count, is responsible for the monotonic increase of T_c in $Mn_{2-x}Fe_xB$ [12,15]. The DOS calculations in Fig. 5a and b are based on the Mn_2B unit cell in Fig. 5c with Mn or Fe on the 8*h* Wyckoff site, respectively. To

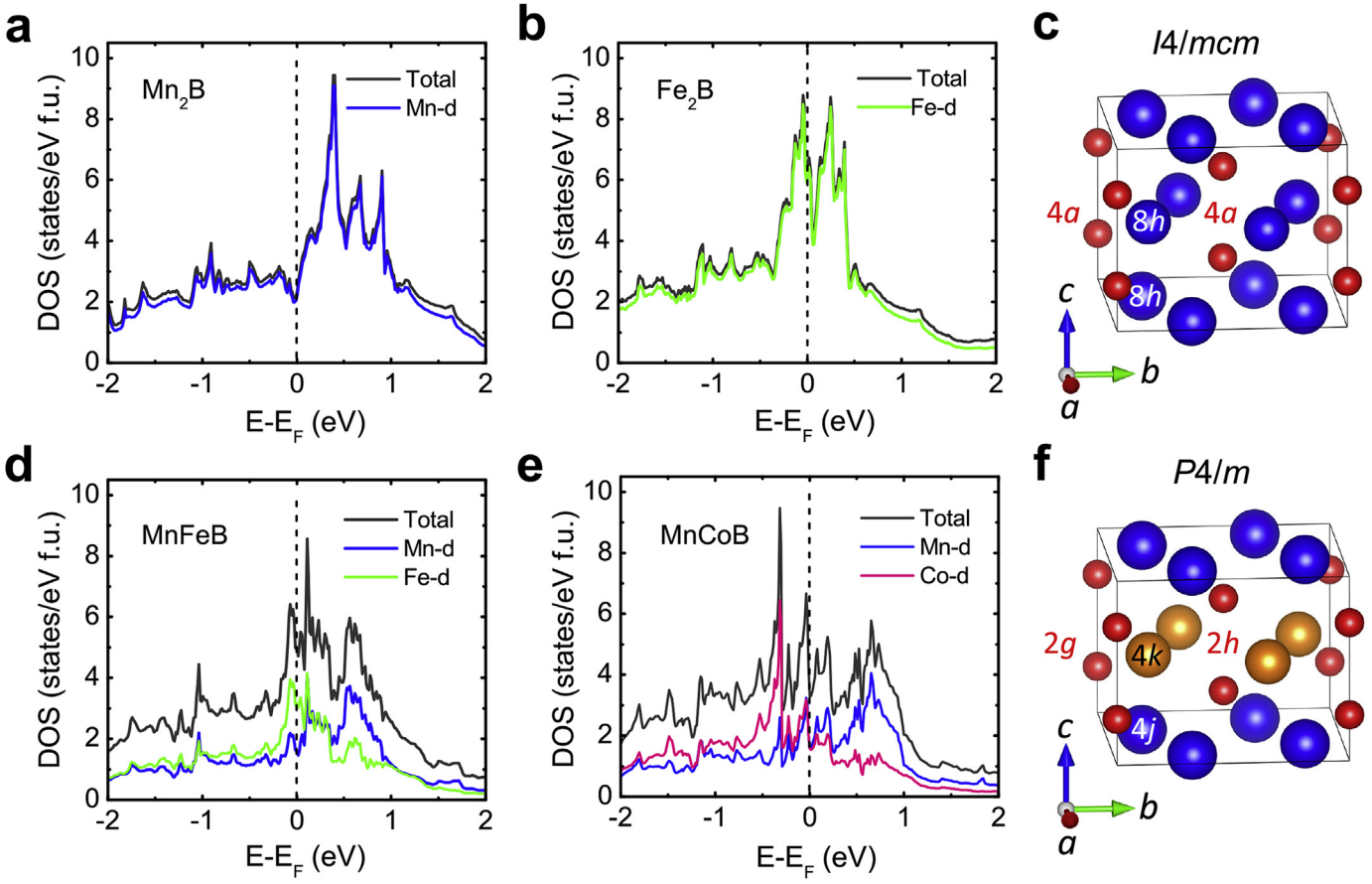

Fig. 5. Density of states plotted as a function of energy in (a) Mn_2B, (b) Fe_2B, (d) MnFeB, and (e) MnCoB. (c) shows the unit cell used to calculate DOS in (a,b), and (f) shows the unit cell for the calculations in (d,e).

explain the non-monotonic behavior of T_c and M_s in $Mn_{0.95-\delta}Fe_{1.05+\delta-x}Co_xB$, we calculated DOS for two limiting compositions, namely MnFeB and MnCoB. Fig. 5f shows that the structural input for these calculations was based on the Mn_2B unit cell but with a 50/50 mixture of Mn/Fe or Mn/Co on the 8*h* Wyckoff site. Subsequently, the space group symmetry was lowered from *I*4 /*mcm* to *P*4 /*m* with Mn atoms on the 4*j* site and Co/Fe on the 4*k* site (Fig. 5f). The resulting DOS plots for MnFeB and MnCoB are presented in Fig. 5d and e. In the former, the main contribution to the largest Van Hove singularity is from the Fe *d*-states, whereas in the latter, it is from the Co *d*-states. Note that E_F is located before/after the largest Van Hove singularity in MnFeB/MnCoB which explains the non-monotonic dome-shape dependence of both T_c and M_s on the Co content in Fig. 4c,f. Substitution of Fe by Co in MnFeB, or Co by Fe in MnCoB, leads to the increase or decrease of electron count and consequently to the positive and negative shift of E_F in a narrow region around the Van Hove singularity. Therefore, the non-monotonic change of T_c and M_s in $Mn_{0.95-\delta}Fe_{1.05+\delta-x}Co_xB$ results from the specific structure of DOS around E_F in these three-metal boride alloys. In contrast, the simple DOS structures of two-metal alloys, $Mn_{2-x}Fe_xB$, in Fig. 5a and b result in a monotonic change of T_c [12,15]. Note that the model in Fig. 5f has a structural order, whereas the absence of superstructure peaks in our X-ray patterns (Fig. 3) confirm a homogeneous distribution of atoms and a lack of such order. Therefore, to validate our DOS results, we performed another calculations in the Supplementary Information with a different atomic arrangement and confirmed that the results remain unchanged.

4. Conclusions

The main objective of this work is to introduce three-metal boride alloys based on the M_2B structure and tune their magnetic properties. EDX analysis shows that the $Mn_{0.95-\delta}Fe_{1.05+\delta-x}Co_xB$ alloys ($\delta = 0 - 0.15$ and $x = 0 - 1.05$) have a small Mn deficiency with respect to the nominal composition. The Mn deficiency is consistent with the formation of Mn-rich MB impurity which is removed by acid treatment. Analysis of PXRD data reveals a statistical mixture of Mn, Fe, and Co on the 8*h* Wyckoff site of the M_2B structure. Lattice parameters show an anisotropic variation with *x*. The ferromagnetic transition temperature T_c and the saturated moment M_s show a non-monotonic and parallel dependence on *x*. This behavior results from a non-monotonic variation of $N(E_F)$ by increasing the electron count in $Mn_{0.95-\delta}Fe_{1.05+\delta-x}Co_xB$. The magnetocaloric effect is maximum where T_c and M_s are maximum, at $x = 0.84$ ($Mn_{0.80}Fe_{0.36}Co_{0.84}B$). The three-metal boride alloys presented here set the stage for the formation of high-entropy alloys in th M_2B series similar to recent reports in the MB_2 family (with AlB_2 structure) [24].

Acknowledgments

This work was funded by the National Science Foundation, award No. DMR-1708929.

Appendix A. Supplementary data

Supplementary data to this article can be found online at https://doi.org/10.1016/j.jallcom.2019.07.119.

References

[1] R. Kiessling, The borides of manganese, Acta Chem. Scand. 4 (21) (1950) 146.
[2] G. Akopov, M.T. Yeung, R.B. Kaner, Rediscovering the crystal chemistry of borides, Adv. Mater. 29 (21) (2017) 1604506.
[3] J.P. Scheifers, Y. Zhang, B.P.T. Fokwa, Boron: enabling exciting metal-rich structures and magnetic properties, Acc. Chem. Res. 50 (9) (2017) 2317–2325.
[4] X. Tan, P. Chai, C.M. Thompson, M. Shatruk, Magnetocaloric effect in $AlFe_2B_2$: toward magnetic refrigerants from earth-abundant elements, J. Am. Chem. Soc. 135 (25) (2013) 9553–9557.
[5] S. Hirt, F. Yuan, Y. Mozharivskyj, H. Hillebrecht, $AlFe_{2-x}Co_xB_2$ (x=0-0.30): T_c Tuning through Co substitution for a promising magnetocaloric material realized by spark plasma sintering, Inorg. Chem. 55 (19) (2016) 9677–9684.
[6] G. Akopov, L.E. Pangilinan, R. Mohammadi, R.B. Kaner, Perspective: superhard metal borides: a look forward, Apl. Mater. 6 (7) (2018) 070901.
[7] Q. Gu, G. Krauss, W. Steurer, Transition metal borides: superhard versus ultra-incompressible, Adv. Mater. 20 (19) (2008) 3620–3626.
[8] E.E. Havinga, H. Damsma, P. Hokkeling, Compounds and pseudo-binary alloys with the $CuAl_2$ (C_{16})-type structure I. Preparation and X-ray results, J. Less Common Met. 27 (2) (1972) 169–186.
[9] R. Masrour, E.K. Hlil, M. Hamedoun, A. Benyoussef, O. Mounkachi, H.E. Moussaoui, Structural, electronic and magnetic properties of MnB_2, Bull. Mater. Sci. 38 (4) (2015) 1065–1068.
[10] A.K. Iyer, Y. Zhang, J.P. Scheifers, B.P.T. Fokwa, Structural variations, relationships and properties of M2B metal borides, J. Solid State Chem. 270 (2019) 618–635.
[11] H. Kadomatsu, F. Ishii, H. Fujiwara, Magnetization, lattice constants and hydrostatic pressure effect on the curie temperature of $(Co_{1-x}Mn_x)_2B$, J. Phys. Soc. Jpn. 47 (4) (1979) 1078–1085.
[12] A.S. Schaafsma, M.J. Besnus, I. Vincze, F. Van Der Woude, Effect of Mn on the magnetic moments of Fe in intermetallic compounds, J. Magn. Magn. Mater. 15–18 (1980) 1149–1150.
[13] A. Edström, M. Werwiński, D. Iuşan, J. Rusz, O. Eriksson, K.P. Skokov, I.A. Radulov, S. Ener, M.D. Kuz'min, J. Hong, M. Fries, D.Y. Karpenkov, O. Gutfleisch, P. Toson, J. Fidler, Magnetic properties of $(Fe_{1-x}Co_x)_2B$ alloys and the effect of doping by 5d elements, Phys. Rev. B 92 (17) (2015) 174413.
[14] M.C. Cadeville, E. Daniel, Sur la structure électronique de quelques borures d'éléments de transition, J. Phys. 27 (7–8) (1966) 449–457.
[15] M. Fries, Phase Transitions of Borides and Phosphides for Application in Magnetic Energy Conversion, Ph.D. Thesis, Technische Universität, Darmstadt, 2017.
[16] L. Akselrud, Y. Grin, WinCSD: software package for crystallographic calculations (Version 4), J. Appl. Crystallogr. 47 (2) (2014) 803–805.
[17] N. Kinami, K. Wakiya, M. Uehara, J. Gouchi, Y. Uwatoko, I. Umehara, Magnetocaloric effect in single-crystal HoNi with a canted magnetic structure, Jpn. J. Appl. Phys. 57 (10) (2018) 103001.
[18] R. Tank, O. Jepsen, A. Burkhardt, O.K. Andersen, The STUTTGART TB-LMTO-ASA Program, Max-Planck-Institut fur Festkorperforschung, Stuttgart, Germany, 1999 version 4.7.
[19] Y. Kuz'ma, M. Chepiga, A. Plakhina, Phase equilibria in the Cr-Co-B, Mn-Fe-B, and Mn-Co-B systems, Inorg. Mater. 2 (1966) 1038–1043.
[20] C. Kapfenberger, B. Albert, R. Pöttgen, H. Huppertz, Structure refinements of iron borides Fe_2B and FeB, Z. für Kristallogr. - Cryst. Mater. 221 (5–7) (2006) 477–481.
[21] Y.Q. Chen, J. Luo, J.K. Liang, J.B. Li, G.H. Rao, Magnetic properties and magnetocaloric effect of $Nd(Mn_{1-x}Fe_x)_2Ge_2$ compounds, J. Alloy. Comp. 489 (1) (2010) 13–19.
[22] V.K. Pecharsky, J. Gschneidner, K.A., Giant magnetocaloric effect in $Gd_5(Si_2Ge_2)$, Phys. Rev. Lett. 78 (23) (1997) 4494–4497.
[23] O. Tegus, E. Brück, K.H.J. Buschow, F.R. de Boer, Transition-metal-based magnetic refrigerants for room-temperature applications, Nature 415 (6868) (2002) 150–152.
[24] J. Gild, Y. Zhang, T. Harrington, S. Jiang, T. Hu, M.C. Quinn, W.M. Mellor, N. Zhou, K. Vecchio, J. Luo, High-entropy metal diborides: a new class of high-entropy materials and a new type of ultrahigh temperature ceramics, Sci. Rep. 6 (2016) 37946.